15

Laser Drilling Assisted with Jet Electrochemical Machining

Hua Zhang
School of Mechanical Engineering, Nantong University, Nantong, Jiangsu
China

1. Introduction

Laser drilling is a noncontact, precise and reproducible technique that can be used to form small diameter and high-aspect ratio holes in a wide variety of materials. Laser drilling is most extensively used in the aerospace, aircraft, and automotive industries. The most important application of laser drilling in the aerospace industry is the drilling of a large number of closely spaced effusion holes with small diameter and high quality to improve the cooling capacity of turbine engine components. Drilling rates as high as 100 holes/s can be achieved in production environment by coordinating the workpiece motions with pulse period of pulsed laser source. Laser drilling does not pose substantial problems at high angles of incidences. Laser drilling is also well suited for the nonconducting substrates or metallic substrates coated with nonconducting materials where the electric discharge machining is limited. In addition, recently the laser drilling of composite materials such as multilayer carbon fiber composites for aircraft applications is attracting increasing interest due to potential advantages of rapid processing, absence of tool wear, and ability to drill high-aspect ratio holes at shallow angles to the surface.

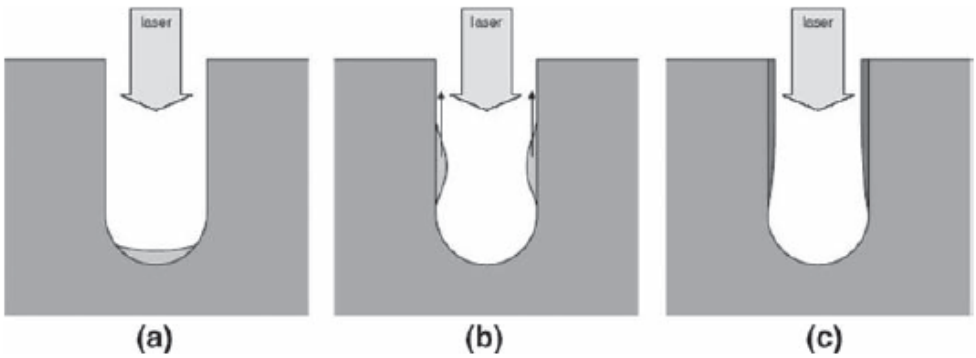

Fig. 1. Physical processes during percussion laser drilling. (a) Melt pool formation (b) splashing out of molten material, and (c) formation of recast layer.

The physical processes occurring during laser drilling are shown in Fig.1. The process can be split up into three stages. Initially a thin region of molten material is formed by absorption

of laser energy at target surface. After some time the surface of this melt pool reaches vaporization temperature. The sudden expansion of the vapor evaporating from the surface eventually leads to the splashing stage when the melt pool is pushed radially out by the recoil pressure. Melt expulsion occurs when the pressure gradients on the surface of the molten material from the hole. On its way of escaping out some part of this molten material may re-solidify at the wall. These molten materials re-solidify adhering to the sidewall of the hole as a thin layer referred to as the 'recast layer'. Also, often spatter of molten material on the surface surrounding the entrance and exit of the hole will occur during the laser drilling process. The spatter and recast layer are defects of laser drilling and limit the application. Therefore, the elimination of these defects is one subject of intense research in laser machining.

This chapter contains a new typical hybrid process of laser drilling assisted with jet electrochemical machining (JECM-LD) for the minimization of recast and spatter.

2. Principle

JECM-LD combines two different sources of energy simultaneously: energy of photons (laser drilling) and energy of ions (ECM). The main aim of combining a jet electrolyte with laser beam is to obtain high process quality by reducing the recast layer and spatter produced in laser drilling. The jet electrolyte is aligned coaxially with a focused laser beam and creates a noncontact tool-electrode. The focused laser beam and the jet electrolyte are acting on the same surface of workpiece synchronously.

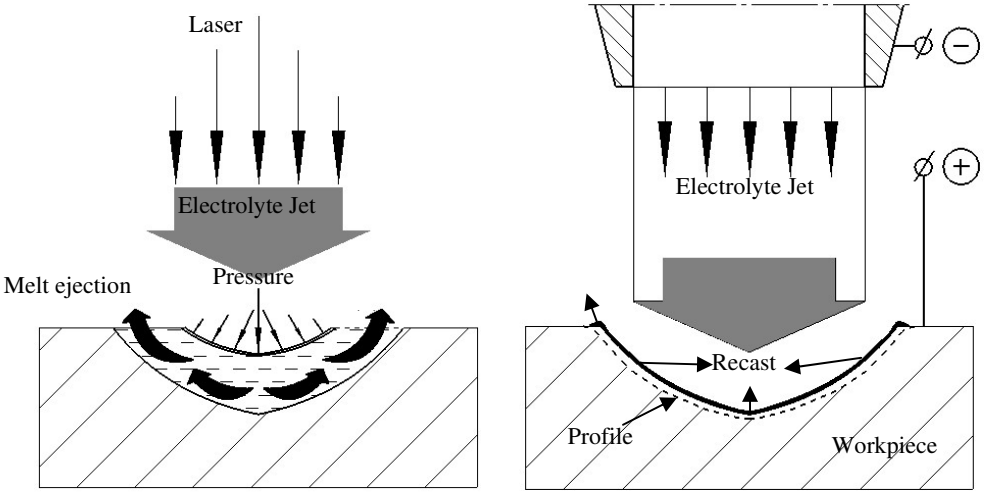

(a) In pulse width (b) In the inter-pulse

Fig. 2. Principle scheme of JECM-LD

In the course of JECM-LD, material is removed mainly by laser drilling in pulse width. The defects are overcome by the effect of jet electrolyte which consists of effective cooling to workpiece, transporting debris and electrochemical reaction with materials in the inter-pulse of laser. Fig.2 illustrates the principles of JECM-LD.

3. Measurement of laser attenuation in electrolyte

JECM-LD aligns a jet electrolyte coaxially with a laser beam. The laser beam needs to transmit in the jet electrolyte before being focused on the machining area. Electrolyte is a neutral salt solution, which is attenuable to laser energy by absorption and scattering. The property of laser attenuation in electrolyte is the key factor of JECM-LD.

3.1 Theoretical background

Electrolyte is a neutral salt solution with the solute of sodium salt and the solvent of pure water. The solution has a number of particles such as water molecules, metallic ions and suspended matter. These particles have significant effects on the laser attenuation in the electrolyte with absorption and scattering. The total attenuation coefficient $\mu(\lambda)$ of solution is given by

$$I_x(\lambda) = I_0(\lambda)\exp[-\mu(\lambda)x] \tag{1}$$

Where $I_0(\lambda)$ is a source of intensity and $I_x(\lambda)$ is the intensity transmitted a distance x in solution. The total attenuation coefficient is the sum of the absorption and scattering coefficients. In terms of the absorption coefficient $\alpha(\lambda)$ and the total scattering coefficient $\beta(\lambda)$, $\mu(\lambda)$ can been written as

$$\mu(\lambda) = \alpha(\lambda) + \beta(\lambda) \tag{2}$$

The absorption coefficient is correlative with the refraction of solution. The index of refraction $n(\lambda)$ and the extinction coefficient $k(\lambda)$ of solution are, respectively, the real and imaginary parts of its spectral complex refractive index is written as

$$\vec{n}(\lambda) = n(\lambda) - ik(\lambda) \tag{3}$$

The absorption coefficient $\alpha(\lambda)$ is determined by $k(\lambda)$ and the expression is given by

$$\alpha(\lambda) = 4\pi k(\lambda) / \lambda \tag{4}$$

The total scattering coefficient includes two parts of Rayleigh scattering coefficient $\beta_R(\lambda)$ and Mie scattering coefficient $\beta_M(\lambda)$, which can be written as

$$\beta(\lambda) = \beta_R(\lambda) + \beta_M(\lambda) \tag{5}$$

The scattering coefficient is determined by the radius of the particles in solution. A dimensionless parameter q ($q = 2\pi R / \lambda$) is used to be token of particle size. When $q < 0.1$, the scattering is Rayleigh scattering, contrariwise, which is Mie scattering. The electrolyte of this work is an industrial reagent of sodium chloride or sodium nitrate. The electrolyte has different sizes (Radius: 5~10μm) suspended particles result from undissolved matters involved in the industrial reagent. With the higher concentration, the solution has more suspended particles and the effect of scattering is more evident. So the laser attenuation in electrolyte is directly affected by the concentration of solution. The temperature of solution

is also a factor to influence the attenuation coefficient. Here two parameters of Ψ_C and Ψ_T are used to represent the influence of the concentration and temperature, then Eq. (1) can be deduced a new expression

$$I_x(\lambda) = I_0(\lambda)\exp\{-[\alpha(\lambda) + \beta_M(\lambda) + \Psi_C(\mathrm{C} - \mathrm{C}_0) + \Psi_T(T - \mathrm{T}_0)]x\} \tag{6}$$

3.2 Measurement and results

A measurement of laser attenuation in electrolyte has been carried out based on the theoretical analysis mentioned above. The laser systems used in the measurement are a CW semiconductor green laser (wavelength: 532 nm) and a pulsed Nd:YAG laser (wavelength: 1064 nm). The other equipments include a sample quartz glass cell, a heater and a photometer. The sample electrolytes are the neutral sodium solution. The solutes are industrial sodium chloride (Standard no.QB2238.2- 2005 of China National Light Industry Council) and industrial sodium nitrate (Standard no.GBT4553-2002 of China). The concentration of the solution is in terms of linear increase with 2%, 8%, 14% and 20%.

During the measurement, the first step is measuring the source intensity of laser transmitted in the empty sample cell and the result is taken as I_0, then measured the intensity I_x transmitted a distance x in sample solution with different concentration and temperature. Finally, it is straightforward to invert Eq. (6) and find the attenuation coefficient $\mu(\lambda)$, the concentration influence coefficient Ψ_C and the temperature influence coefficient Ψ_T.

Fig.3 shows a light path of green laser transmitting in electrolyte. The brightness of the path is higher with the increase of the solution concentration, which is result of scattering of suspended particles in the electrolyte. It's shown that the reason of green laser attenuation in the electrolyte is mainly scattering.

Figs.4 (a) and (b) show, respectively, the variety of green laser and infrared laser attenuation coefficient in electrolyte at 25℃. It is shown that the laser attenuation coefficient is linear with increase of concentration.

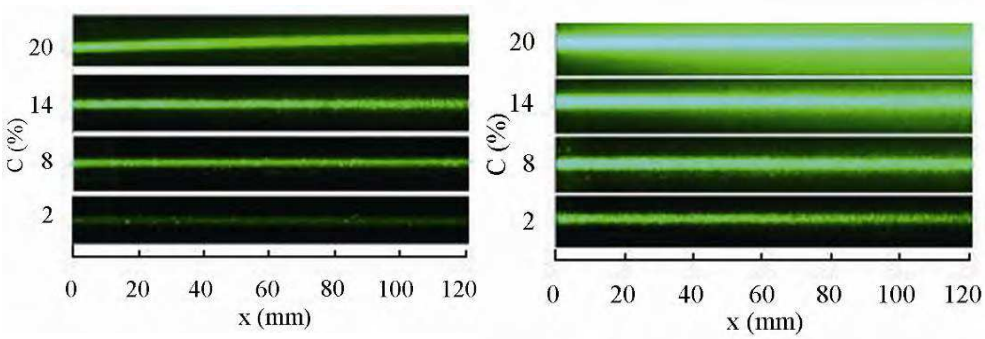

(a) (b)

Fig. 3. Light path of green laser propagation in electrolyte (a) in sodium chloride electrolyte; (b) in sodium nitrate electrolyte

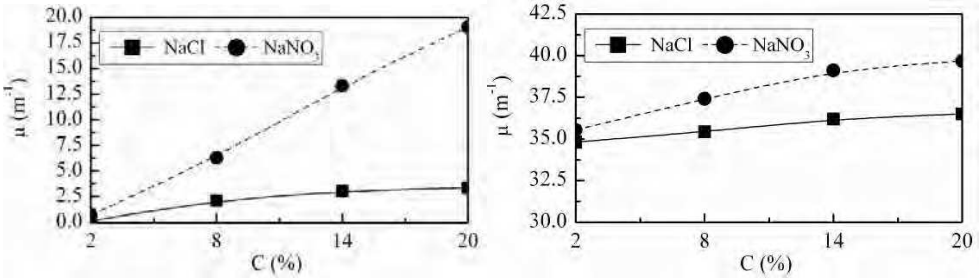

Fig. 4. Attenuation coefficient for electrolyte vs. laser: (a) green laser; (b) infrared laser.

Pure water is most transparent to the visible laser, especially, to green-blue laser of wavelength in the range 470–560 nm. Absorption of infrared laser in pure water is evident. The absorption coefficients of green laser (532 nm) and infrared laser (1064 nm) are 0.0355 and 34.2438m^{-1} respectively. It is shown that the attenuation of green laser in the electrolyte is mainly due to scattering; however, infrared laser is absorbed in electrolyte compared with pure water. The infrared laser attenuation coefficients in various concentrations of electrolyte are higher than 34.5m┐1. Thus the preferred laser in JECM-LD is the green laser or ultrashort infrared laser with high power density.

4. Measurement of mechanical effects during pulsed laser and metals interaction in neutral solution

JECM-LD can be added on purpose to gain better results: to avoid redeposition of debris, to cool the material, or to increase plasma pressure. The improvement of plasma pressure is a major physical phenomenon, which is the reason of mechanical effect during JECM-LD.

4.1 Principle of test on mechanical of laser in neutral solution

As shown in Fig.5, a test setup is comprised of optical parts and measuring parts. A pulsed Nd: YAG laser was used operating at two wavelengths of 1064nm and 532nm. The neutral

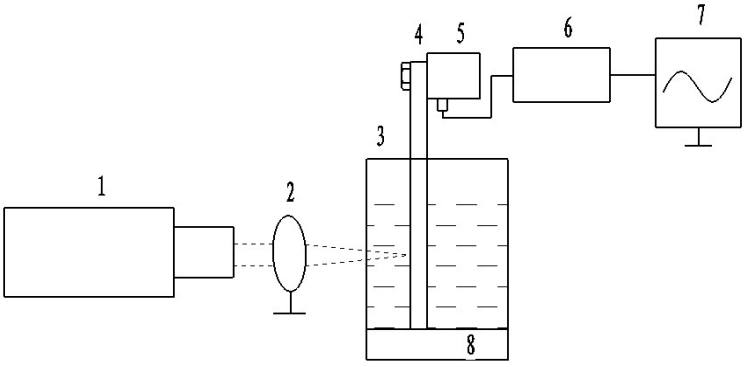

Fig. 5. Schematic diagram of test setup for mechanical effect of laser and metal interaction
1. Laser 2. Lens 3. Quartz glasses sink 4. Metal target 5. Piezoelectric accelerometer 6. Charge amplifier 7. Oscilloscopes 8. Base

solution is sodium nitrate solution and the concentration is 20%. The focal length of lens is 100mm. The thickness of metal target is 0.5mm. The metal target is fixed on the base in quartz glasses tank and forms a cantilever. A piezoelectric accelerometer is fixed on the free end of the cantilever to detect vibration acceleration signals. These signals are output on the oscilloscope through a charge amplifier.

When a pulsed laser is focused on axis position of the cantilever, the laser pulse will produce an instant pressure on the target. Then the cantilever makes a lateral vibration, as shown in Fig.6.

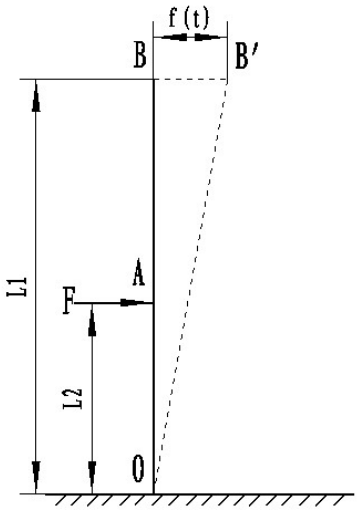

Fig. 6. Schematic diagram of vibrating cantilever

The piezoelectric accelerometer is comprised of piezoelectric element, mass, preload spring, et al. It has the same vibration as the cantilever, and then the piezoelectric element is loaded with an inertia force of the mass. According to Newton's Second Law, the inertia force is written as,

$$F = m \cdot a \tag{7}$$

Where F is inertia force, a is acceleration.

According to vibration theory, the cantilever can be seen as a freedom vibration system with a single degree, the movement of free end can be describe as,

$$f(t) = A_0 \cdot e^{-\beta t} \sin(\omega_n t + \varphi) \tag{8}$$

Where A_0 is initial amplitude, β is damping coefficient, ω_n is natural frequency, φ is initial phase angle. The acceleration of free end can be obtained by the second differential equation (8),

$$a(t) = (\beta^2 A_0 e^{-\beta t} + A_0 e^{-\beta t} {\omega_n}^2) \sin(\omega_n t + \varphi) - 2\beta A_0 e^{-\beta t} \omega_n \cos(\omega_n t + \varphi) \tag{9}$$

When t=0, the acceleration of free end is the maximum,

$$a_{\max} = (\beta^2 + \omega_n{}^2)A_0 \tag{10}$$

Initial amplitude A_0 is the maximum deformation of the cantilever. According to mechanics of materials, A_0 should be written as,

$$A_0 = \frac{FL_2{}^2}{3EI}(3L_1 - L_2) \tag{11}$$

Where E is modulus of elasticity, I is moment of inertia. Substitution of equation (11) into equation (10) yields,

$$a_{\max} = F \cdot (\beta^2 + \omega_n{}^2)\frac{L_2{}^2}{3EI}(3L_1 - L_2) \tag{12}$$

Because β and ω_n are constant, the impact force has certain proportion to the maximum acceleration. Used $K_a = \frac{L_2{}^2}{6EI}(3L_1 - L_2)(\beta^2 + \omega_n{}^2)$ as a constant, equation (12) can be written as,

$$a_{\max} = K_a \cdot F \tag{13}$$

According to the piezoelectric effect, the charge generated by the piezoelectric element has a certain proportion to the acceleration of the free end,

$$q_{\max} = S_q \cdot a_{\max} \tag{14}$$

Where, S_q is charger sensitivity. According to theory of circuit, the output of the charge amplifier is calculated as function of charge q with the following equation,

$$U_0 = -\frac{q}{C_f} \tag{15}$$

Where, C_f is feedback capacitance. Substitution of equation (13) and (14) into equation (15) yields,

$$U_0 = -\frac{S_a K_a}{C_f} F \tag{16}$$

Therefore, the value of signal on oscilloscope can be used to calculate the impact force by the laser and metal interaction.

4.2 Measurement and results

Fig.7 and Fig.8 show, respectively, the mechanical signals of pulsed green laser and infrared laser interactived with metal. The environments included being in air, being under $NaNO_3$ solution with depth 2mm and 20mm. Used laser energy per pulse is 150mJ. It is shown that

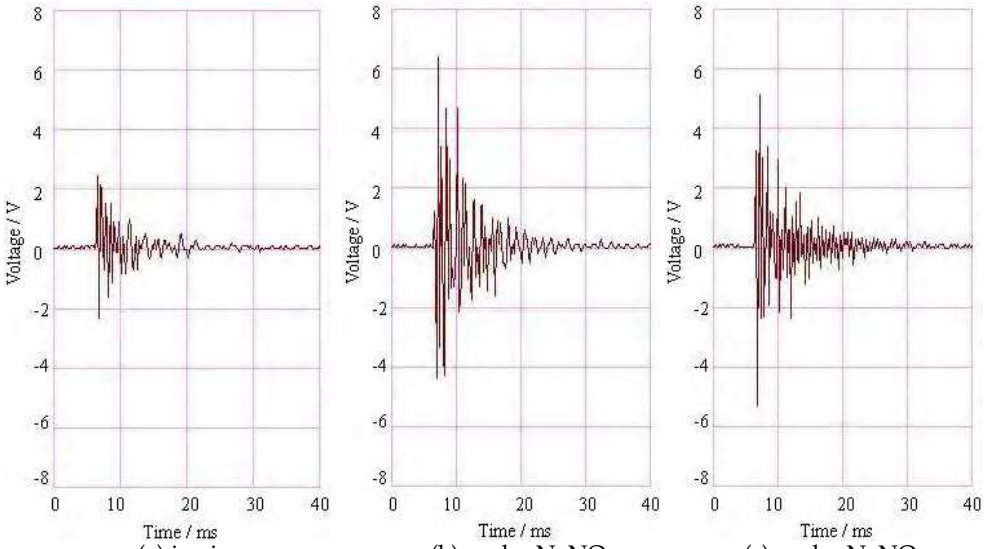

(a) in air (b) under $NaNO_3$ solution(depth=2mm) (c) under $NaNO_3$ solution(depth=20mm)

Fig. 7. Mechanical signals of pulsed green laser and metal interaction (150mJ/per pulse)

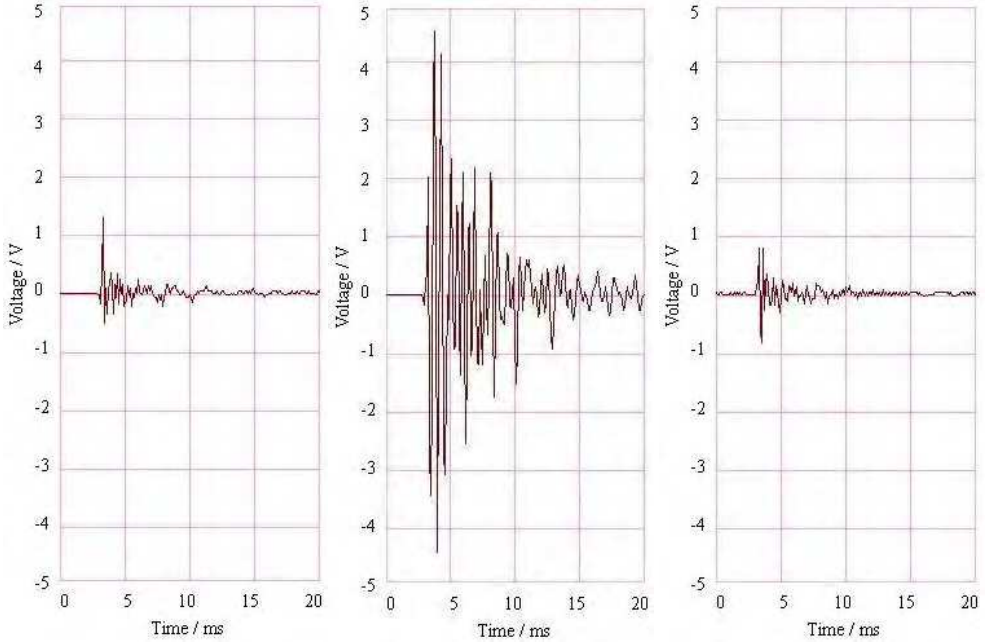

(a) in air (b) under $NaNO_3$ solution(depth=2mm) (c) under $NaNO_3$ solution(depth=20mm)

Fig. 8. Mechanical signals of pulsed infrared laser and metal interaction (150mJ/per pulse)

much higher pressure plasma is formed through the interaction between the laser pulse and metal under neutral solution than in air. The mechanical effect during pulsed laser and stainless target interaction in neutral solution is more than three times higher than in air.

It is also shown that the pressure of the target with infrared laser is decreased with the distance of laser propagation in neutral solution. However, the effect with green laser is stable in the laser transmission range of 20mm. The most probable reason for this is infrared laser is absorbed in neutral solution, but green laser is a case of low absorption. Therefore, the green laser is more suitable for JECM-LD.

5. Modeling of JECM-LD

5.1 Theoretical analysis

Theoretical analysis of JECM-LD is performed by changing machining conditions. There are two conditions in JECM-LD: One is an electrolyte-jet-guided focused pulsed laser with a pulse width of 0.2ms and a frequency of 5Hz. The other is only an electrolyte during the inter-pulse. Fig.9 presents the main idea for the theoretical analysis.

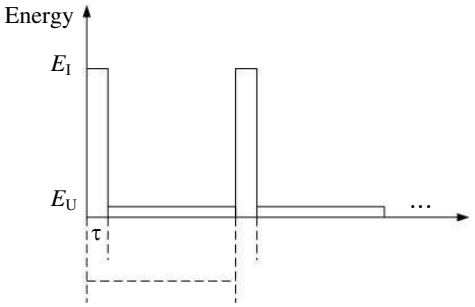

Fig. 9. Schematic diagram of the energy to be used for JECM-LD

As the laser pulse width constitutes only one percent of the inter-pulse and the electrical energy is much lower than laser energy in pulse width, the main process energy E is the heat energy E_I of pulsed laser during the pulse width τ. In contrast, the process energy E of the inter-pulse (1/f-τ) is the electrical energy E_U of electrical charge flow. The processes comprising both laser drilling and jet electrochemical machining unceasingly proceeds during JECM-LD, so the theoretical model of JECM-LD should embrace the two kinds of reactions.

5.2 Mathematical model of electrolyte-jet-guided laser drilling

Since the electrolyte-jet-guided laser drilling is quite different from laser drilling in air, the following assumptions should be made pertinent to the effects of the electrolyte jet and the temperature dependent material properties:

1. The melting temperature of the material under study is the maximum temperature the work-piece can reach.
2. The material possesses constant thermal properties.

3. The evaporated material does not interfere with the laser beam, and the scattering of laser radiation within the hole can be neglected.

Suppose that the top surface of the workpiece made of stainless plate is located at the plane z = 0 and the plate is exposed at time t = 0 to the electrolyte jet guided laser. Fig.10 schematically illustrates the cylindrical coordinate system.

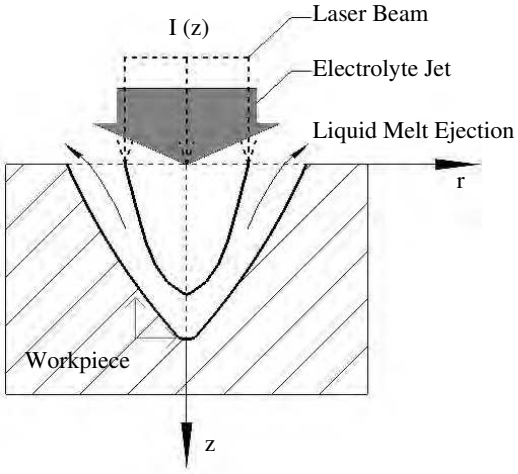

Fig. 10. Schematic diagram of the model for JECM-LD process

To elucidate the evolution of the temperature field, the time-dependent heat conduction equation is solved in the workpiece domain under the appropriate boundary conditions. The governing equation in terms of temperature T is

$$\rho c \frac{\partial T}{\partial t} = \nabla[k \nabla T] + Q \tag{17}$$

Where ρ is the material density, c the heat capacity, t the machining time, k the heat conductivity and Q the laser heat source term. In the cylindrical coordinate system, Eq. (1) can be written into

$$\rho c \frac{\partial T}{\partial t} = k\left[\frac{\partial^2 T}{\partial r^2} + \frac{1}{r}\frac{\partial T}{\partial r} + \frac{\partial^2 T}{\partial z^2}\right] + Q \tag{18}$$

The general laser heat source Q can be expressed by

$$Q = -\frac{\partial I(z)}{\partial z} \tag{19}$$

Where $I(z)$ is the intensity of the laser beam incident upon the top workpiece surface from a given distance, z. In the case of metals, $I(z)$ can be quantified according to the Lambert's Law,

$$I(z) = \varepsilon I(0) e^{-\beta z} \tag{20}$$

Where ε is the surface emissivity, β the absorption coefficient. From Eq. (19) and Eq. (20), Q can be written into

$$Q = \varepsilon \beta I(0) e^{-\beta z} \tag{21}$$

Inserting Eq. (21) into Eq. (17) yields

$$\rho c \frac{\partial T}{\partial t} = k \left[\frac{\partial^2 T}{\partial r^2} + \frac{1}{r} \frac{\partial T}{\partial r} + \frac{\partial^2 T}{\partial z^2} \right] + \varepsilon \beta I(0) e^{-\beta z} \tag{22}$$

As the heat loss due to convection and radiation would take place at the top workpiece surface resulting from the cooling by the electrolyte jet, the boundary condition can be expressed by

$$-k \left(\frac{\partial T}{\partial z} \right)_{z=0} = h_c (T - T_a) + \varepsilon \sigma (T^4 - T_a{}^4) \tag{23}$$

Where h_c is the convection coefficient, T_a the ambient temperature and σ the Stephan-Boltzman constant.

The scraps of the workpiece would be carried away in molten state by the electrolyte jet whenever and wherever the material has reached the melting temperature. Thus, for this model, the isotherm line, which represents the melting temperature of the material, can be considered as the profile of the hole during electrolyte-jet-guided laser drilling.

5.3 Mathematical model of jet electrochemical machining

During the inter-pulse, with the ending of pulsed laser beam, the electrolyte jet creates a contactless electrode and has electrochemical reactions onto the workpiece-anode. In this way, the recast layers and spatters have been effectively removed by the electrochemical reactions.

Based on the cylindrical coordinate system of the model of electrolyte-jet-guided laser drilling, a two-dimensional model for JECM can be developed as follows:

In order to model the shaping process with a free jet, the following assumptions should be made (see Fig.11).

1. The top boundary is the shape formed by the preceding electrolyte-jet-guided laser drilling.
2. The cross-section of the jet remains constant along the whole length of the jet.
3. The diameter of the electrolyte jet is assumed to be the same as that of the nozzle.
4. The jet is axisymmetric, thus the system can be described as 2D in cylindrical coordinates (r, z).
5. The electrolyte has constant conductivity.

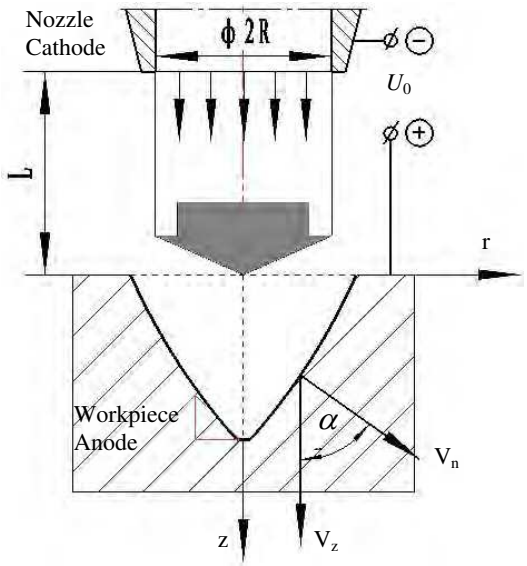

Fig. 11. Schematic diagram of the model for JECM process

Fig.11 shows the change of the shape of the workpiece surface machined by the anodic dissolution as a function of time. During machining, the velocity at which the anodic boundary moves along the *z*-axis is given by

$$V_z = \frac{V_n}{\cos\alpha} \tag{24}$$

Where V_n is the velocity of anodic dissolution, α the angle between the axis of the anode and *z*-axis. The $\cos\alpha$ in Eq.(8), which can be evaluated with the function $z = z_a(r,t)$, describes the shape of the anode as follows:

$$\frac{1}{\cos\alpha} = \sqrt{1+(\frac{\partial z_a}{\partial r})^2} \tag{25}$$

Substituting Eq. (9) into Eq. (8) yields

$$\frac{\partial z_a}{\partial t} = V_n\sqrt{1+(\frac{\partial z_a}{\partial r})^2} \tag{26}$$

The velocity of dissolution V_n can be obtained from the Faraday's Law:

$$V_n = \eta\omega i_a \tag{27}$$

Where, η is the current efficiency of anodic dissolution, ω the equivalent volume of material removed by electrochemical processing and i_a the current density of the anode.

The current density i_a on the anode depends on the distribution of electric potential, u, in the electrolyte, and can be determined from the following Ohm's Law:

$$i_a = \kappa E_a \tag{28}$$

Where κ is the electrolyte electrical conductivity and E_a the electric field intensity at anode given by

$$E_a = |\nabla u|_a \tag{29}$$

Where u is the electrical potential across the gap.

In the case of JECM, the potential between the electrodes, u, can be described by

$$\mathrm{div}(\kappa \,\mathrm{grad}\, u) = 0 \tag{30}$$

By evaluating Eq. (30) in cylindrical coordinates, can be obtained the following equation to define the electric potential distribution:

$$\frac{\partial^2 u}{\partial r^2} + \frac{1}{r}\frac{\partial u}{\partial r} + \frac{\partial^2 u}{\partial z^2} = 0 \tag{31}$$

Eq. (31) can describe the shape of the surface to be machined with the following boundary conditions:

For the cathode-nozzle: $u = 0,$ and $r = r_0$;

For the free surface of jet: $\frac{\partial u}{\partial n} = 0$;

For the anode-workpiece: $z = z_a(r,t)$, $u = U_0$, and

$$\frac{\partial z_a}{\partial t} = \kappa\eta\omega\left|\frac{\partial u}{\partial n}\right|_a \sqrt{1 + (\frac{\partial z_a}{\partial r})^2} \tag{32}$$

With the inter-pulse ending, the reaction of JECM comes to a halt and the result of the model becomes the renewed boundary for the next pulse laser drilling. Thus the two parts of JECM-LD model alternatively work during machining.

6. Simulation and experimental results

6.1 Experimental apparatus

As shown in Fig.12, the JECM-LD apparatus consists of three systems, namely, a laser system, an electrolyte supplying system and a power unit. A stream of electrolyte pumped out of the reservoir flows into the jet cell and meantime joins with a coaxial focused laser beam to form a jet 0.5mm dia. The jet together with the beam strikes against one spot on the workpiece surface. By means of the pump, the pressure of the electrolyte jet can be adjusted within the range of 0-1.5Mpa.

A jet cell with an annular cavity is used to obtain a stable electrolyte jet and slim down the transmitting distance of laser in electrolyte. Fig.13 shows the construction of a jet cell.

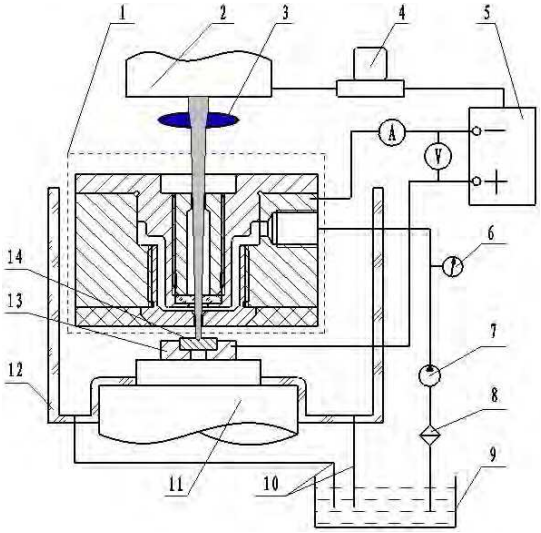

1 Jet cell; 2 Laser system; 3 Focusing lens; 4 Control unit; 5 DC power unit; 6 Pressure gauge; 7 Pump; 8 Filter; 9 Electrolyte reservoir; 10 Back pipelines; 11 CNC Table; 12 Work cell; 13 Holder; 14 Workpiece

Fig. 12. Schematic diagram of JECM-LD system

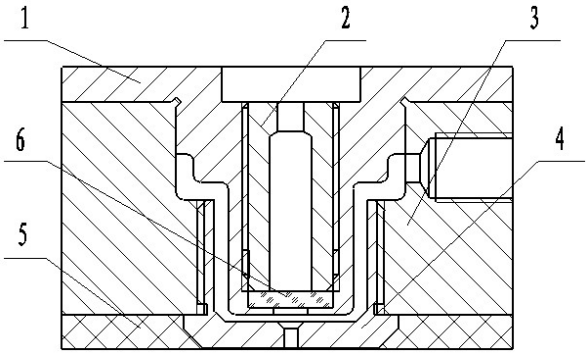

1 Impacted plank; 2 Lock bolt; 3 Base; 4 Nozzle; 5 Insulated layer; 6 Quartz window

Fig. 13. Structure of a jet cell

6.2 Experimental parameters

As a pulse Nd:YAG laser at second harmonic wavelength, it has parameters as follows: wavelength of 532nm; pulse length of 0.2ms; frequency of 5Hz and energy per pulse in the range of 0-300mJ. The workpiece is made of 321 stainless steel 0.5mm thick. Table1 lists the material properties.

A DC power unit with a working voltage in the range of 0-50V and current 5A is adopted in the experiments. The electrolyte from the reservoir on the manifold enters a plunger pump, where it is pumped out at a pressure of 1.5MPa.

Property	Value
Density, ρ [kg·m^{-3}]	7900
Heat conductivity, k [J·m^{-1}·s^{-1}·℃$^{-1}$]	28.5
Heat capacity, C [J·kg^{-1}·℃$^{-1}$]	502
Melting temperature, T_m [℃]	1400
Convection heat transfer coefficient, h_c [W·m^{-2}·℃$^{-1}$]	100
Surface emissivity, ε	0.68
Absorption coefficient, β [m^{-1}]	5×10^3

Table 1. Properties of 321 stainless

In the experiments is used a sodium nitrate electrolyte with a percentage concentration of 18% in weight and a conductivity of 12.2 $(\Omega \cdot \mathrm{m})^{-1}$. The volume electrochemical equivalent of 321 stainless steel is 2.1x10^{-9} $\mathrm{m}^3 / (\mathrm{A} \cdot \mathrm{min})$. The current efficiency is about 0.6. The distance between the nozzle and the workpiece surface is 0.8mm.

6.3 Simulation results

The model of JECM-LD includes two sub-models at different machining stages. One is the sub-model of electrolyte-jet-guided laser drilling and the other of jet electrochemical machining. With the machining stage changing, the simulation is computed with different sub models and the results are summarized step by step.

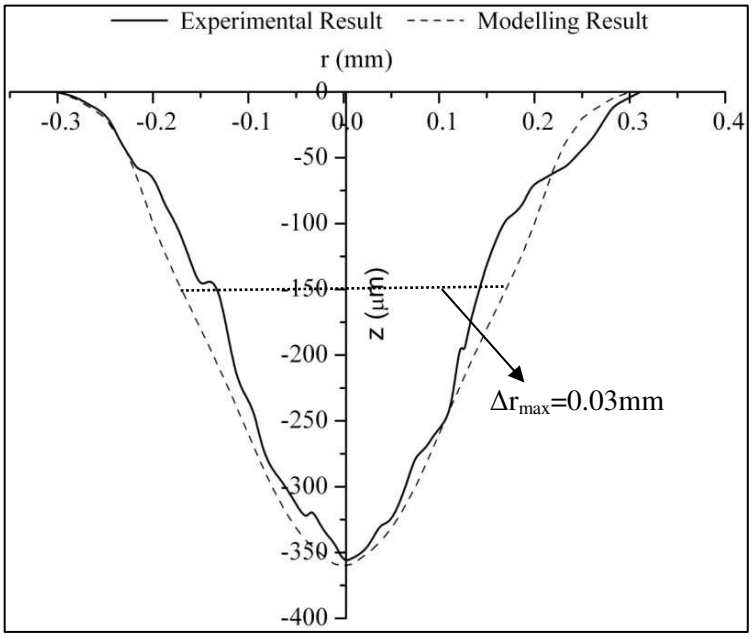

Fig. 14. Simulated and experimental hole cross-sections machined by JECM-LD
(Energy per pulse: 200mJ; ECM voltage: 40V; Electrolyte pressure: 1MPa; Machining time: 10s)

Fig.14 illustrates the shape of the vertical cross-section along the hole-axis from the simulation and from the experiment, which is plotted by means of the three-dimensional profilemeter (MicroXAM, ADE, USA). The comparison of Fig.14 displays a good agreement between the simulated and experimental results in terms of both the hole depth and the shape of the cross-section. However, a noticeable difference exists between the bottom shapes of the simulated cross-section and the experimental one. The former contrasts markedly with the latter by its greater flatness. This might be attributed to the more serious attenuation of laser energy by the scattering and absorption of electrolyte jet.

Therefore, the feasibility of the two-dimensional model is evidenced by the satisfied compliance of the simulated results with the experimental ones.

6.4 Experimental results

In order to make comparison with the laser drilling in air, a millisecond second green laser was used for JECM-LD to work out penetrated holes. The energy per pulse was 200mJ, and the electrochemical machining voltage 40V. The optical microscope was used to examine the experimental results.

As can be seen from Fig.15, for the holes laser-drilled in air, the surfaces both at the entrance and the exit are all encircled by a large irregular area comprising spattering deposits and re-solidified molten layers. In contrast, from Fig.16, it is clear that few spatters could be unveiled on both sites around the hole drilled with JECM-LD. This may be chiefly ascribed to the high-speed electrolyte jet, which effectively cools the material to be processed and discharge scraps. Fig.16 also exhibits better surface quality and a smoother hole periphery, however, an obvious annular electrochemical overcut can be observed at the entrance surface.

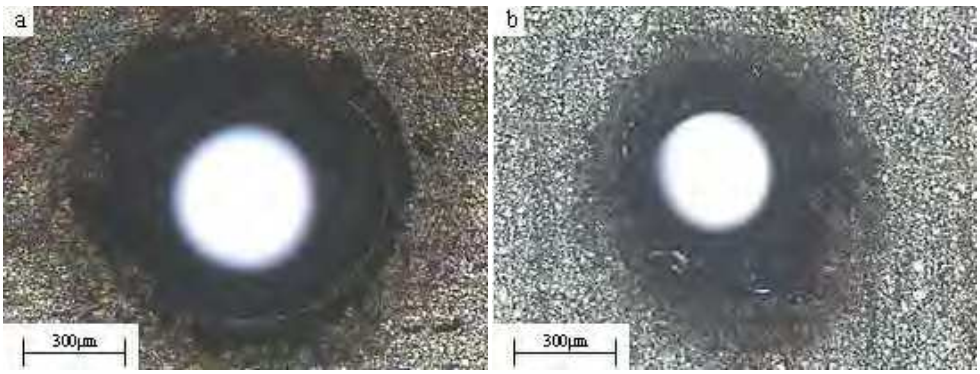

Fig. 15. Micrograph of a penetrated hole drilled with a green laser in air (200mJ, 10s).
(a) Entrance surface; (b) Exit surface

Fig.17 (a) and (b) separately display the details of the exit surface of Fig.15 and Fig.16. Unlike the laser drilling in air(see Fig.17(a)), neither spatters nor recast layers could be discovered on the periphery of the hole drilled with JECM-LD (see Fig.17 (b)). This might be attributed to the electrolyte jet, which rids the recast layers of the surface to be processed.

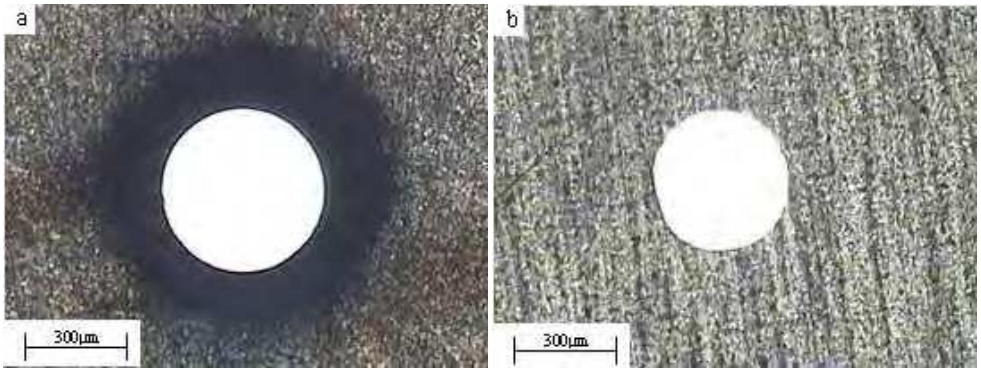

Fig. 16. Micrograph of a penetrated hole drilled with JECM-LD (200mJ, 40V, 20s).
(a) Entrance surface; (b) Exit surface

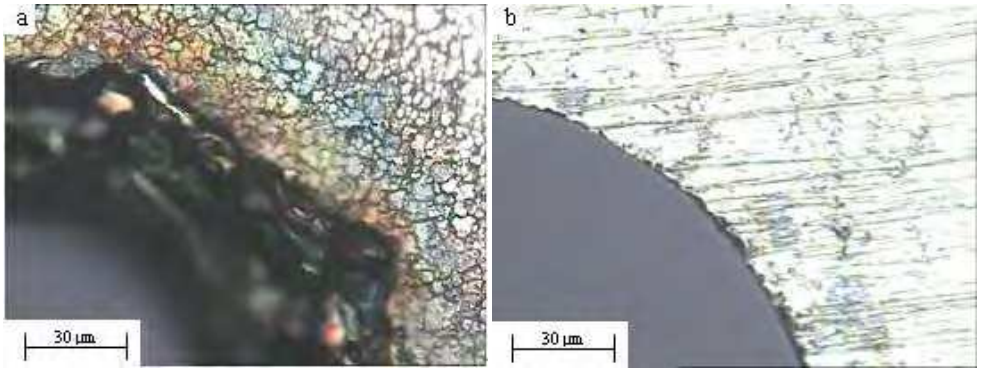

Fig. 17. Micrograph of the peripheral surface of a penetrated hole drilled with different processes.
(a) Laser-drilled in air (200mJ, 10s); (b) JECM-LD (200mJ, 40V, 20s)

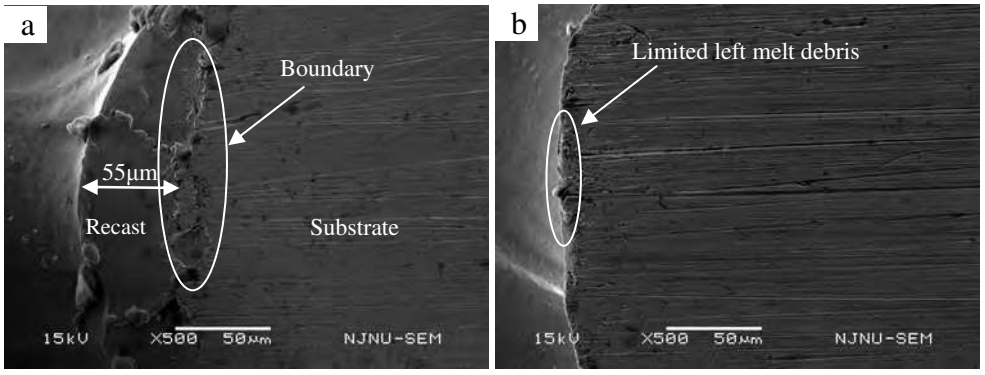

Fig. 18. SEM image of the sidewalls of hole drilled with different process.
(a) Laser drilling in air (200mJ, 10s); (b) JECM-LD (200mJ, 40V, 20s)

The typical cross-sectional view of holes machined with JECM-LD and laser drilling in air are shown in Fig.18. It is shown that there is an obvious boundary between the recast and substrate in Fig.18(a). The thickest recast layer is about 55μm. It is confirmed that recast is an inherent defect associated with holes produced with laser drilling. As can be seen in Fig.18(b), neither boundary nor recast layer can be seen on the sidewalls of hole machined with JECM-LD. There are only few of limited left melt debris adhering to the sidewalls. With comparing the Fig.18(a) and Fig.18(b), the new hybrid process really reduce the recast more than 90% on line.

As the most popularized criterion for defining the cutting efficiency in laser drilling, Material Removal Rate (for short MRR) can be defined as

$$\mathrm{MRR}=\frac{\frac{1}{n}\sum_{i=1}^{i=n}\Delta m_i}{t} \tag{33}$$

Where Δm_i is the lost mass of workpiece in the i-th experiment, n the number of experiments and t the machining time.

Fig.19 evinces the effects of laser pulse energy on MRR and Fig.20 the electrochemical machining voltage on it. These data come from Eq.33 after five repeated experiments with the machining time of 10s each.

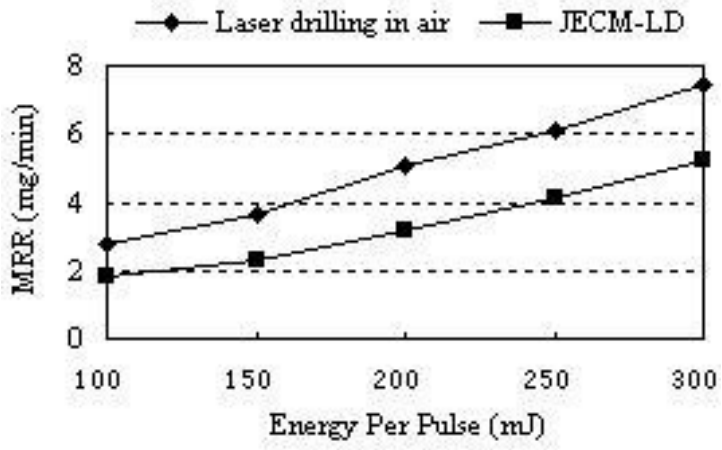

Fig. 19. Effects of energy per pulse on MRR

From Fig.19, it can be seen that MRR increases with the energy per pulse rising. Since a portion of the laser beam has been absorbed and scattered by the electrolyte, the MRR of JECM-LD appears lower than the laser drilling in air, the efficiency of JECM-LD with millisecond green laser is about 70% of laser drilling in air.

Fig.20 shows that MRR remains almost un-changed with the electrochemical machining volt-age increasing. This is because of the insignificant anodic dissolution provided that the voltage is low and the working distance long. It stands to reason that laser beam takes the

chief responsibility for removing scraps from the processed surfaces during JECM-LD, and the jet electrochemical machining plays an auxiliary part in reducing the recast layers and spatters.

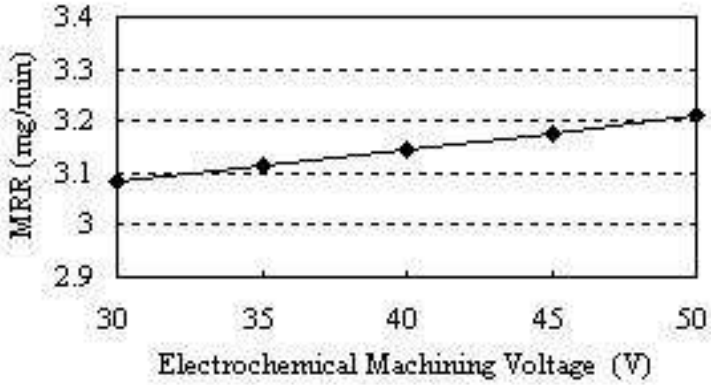

Fig. 20. Effects of ECM voltage on MRR with JECM-LD

7. Conclusions

This work has developed and investigated a novel hybrid process of laser drilling assisted with jet electrochemical machining to improve the quality of laser-drilled holes. The main conclusions can be summarized as follows:

1. The attenuation of green laser in the electrolyte mainly is scattering and the infrared laser is absorbed in electrolyte.
2. Mechanical effect during pulsed laser and stainless target interaction in neutral solution is more than three times higher than in air.
3. Able to effectively reduce the recast layers and spatters, the JECM-LD has an annular electrochemical overcut left behind surrounding the entrance surface after the completion of the process.
4. The laser beam takes the chief responsibility to remove the scraps material during JECM-LD while the jet electrochemical machining serves the auxiliary function of eliminating the recast layers and spatters.
5. The efficiency of JECM-LD with millisecond green laser declines to about 70% of the laser drilling in air.

It is evidenced that the JECM-LD that combines the laser drilling and jet electrochemical machining is on the position to obtain high machining quality with reduced recast layers and spatters. Having great potentiality in eradicating the defects inherent in laser-drilled holes, the hybrid process for hole drilling is expected to become a versatile tool finding broader applications in aerospace and aircraft industries.

8. References

[1] K.T. Voisey, T.W. Clyne. Laser drilling of cooling holes through plasma sprayed thermal barrier coatings. Surface and Coatings Technology, 2004, 176:296-306.

[2] W.S. Rodden, S.S. Kudesia, D.P. Hand, J.D. Jons. Use of "assist" gas in the laser drilling of titanium. Journal of Laser Applications, 2001, 13:204-208.
[3] J.C. Verhoeven, J.K. Jansen, R.M. Mattheij. Modelling laser induced melting. Mathematical and Computer Modelling, 2003, 37:419-437.
[4] Hua Zhang, Jiawen Xu, Jiming Wang. Investigation of a novel hybrid process of laser drilling assisted with jet electrochemical machining. Optics and Lasers in Engineering, 2009, 47(11):1242-1249
[5] H. Zhang, J.W. Xu, J.M. Wang. Green Laser Drilling Assisted with Jet Electrochemical Machining of Nickel-based Superalloy. Key Engineering Materials, 2010, 426-427:75-80.
[6] Zhang Hua, Xu Jiawen. Modeling and Experimental Investigation of Laser Drilling with Jet Electrochemical Machining. Chinese Journal of Aeronautics, 2010, 23(4):454-460.
[7] Hua Zhang, Jiawen Xu, Jianshe Zhao, Guoran Hua. Mechanical effects during pulsed laser and metals interaction in neutral solution. Key Engineering Materials, 2011, 464:623-626.
[8] Hua Zhang, Jiawen Xu, Jianshe Zhao, Guoran Hua. Mechanism of Recast Removal During Laser Drilling Underwater. Advanced Science Letters, 2011, 4(6-7):2071-2075.

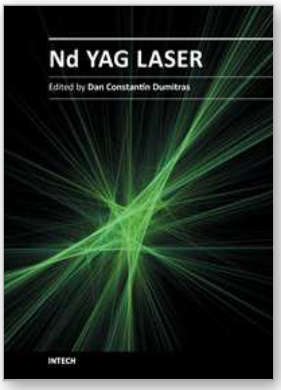

Nd YAG Laser

Edited by Dr. Dan C. Dumitras

ISBN 978-953-51-0105-5
Hard cover, 318 pages
Publisher InTech
Published online 09, March, 2012
Published in print edition March, 2012

Discovered almost fifty years ago at Bell Labs (1964), the Nd:YAG laser has undergone an enormous evolution in the years, being now widely used in both basic research and technological applications. Nd:YAG Laser covers a wide range of topics, from new systems (diode pumping, short pulse generation) and components (a new semiorganic nonlinear crystal) to applications in material processing (coating, welding, polishing, drilling, processing of metallic thin films), medicine (treatment, drug administration) and other various fields (semiconductor nanotechnology, plasma spectroscopy, laser induced breakdown spectroscopy).

INTECH
open science | open minds

InTech Europe
University Campus STeP Ri
Slavka Krautzeka 83/A
51000 Rijeka, Croatia
Phone: +385 (51) 770 447
Fax: +385 (51) 686 166
www.intechopen.com

InTech China
Unit 405, Office Block, Hotel Equatorial Shanghai
No.65, Yan An Road (West), Shanghai, 200040, China
中国上海市延安西路65号上海国际贵都大饭店办公楼405单元
Phone: +86-21-62489820
Fax: +86-21-62489821